Check for updates

ADVANCED FUNCTIONAL MATERIALS
www.afm-journal.de

Sub-Nanometer Porous Carbon Materials for High-Performance Supercapacitors Using Carbon Dots as Self-templated Pore-Makers

Xi-Rong Zhang, Tian-Bing Song, Tian-Le He, Qian-Li Ma, Zhao-Fan Wu, Yong-Gang Wang, and Huan-Ming Xiong**

Customizable porous carbon structures are critical for high-performance electrode materials, and the modulation of the pore parameters at different levels remains a great challenge. For supercapacitors, the preferred carbon materials should own high specific capacitance, nice rate performance, large density, low self-discharge, and high mass-loading, which could be accomplished by sub-nanometer pores (0.5–1.0 nm). Herein, a new method of using carbon dots (CDs) as self-templates is reported to produce porous carbon with uniform pore diameters of 0.64–0.80 nm. As a result, the optimal sample with a high packing density (0.81 g cm^{-3}) displays outstanding capacitances (gravimetric 515.5 F g^{-1}, areal 5.16 F cm^{-2}, and volumetric 417.6 F cm^{-3} respectively at 1 A g^{-1}) at the commercial-level mass-loading of 10 mg cm^{-2}. The assembled high-loading symmetric supercapacitor shows a high energy density of 22.3 Wh kg^{-1} at 3500 W kg^{-1}, as well as a long cycle stability (99.9% of retention rate after 10 000 cycles at 2 A g^{-1}) in an ultrawide voltage range of 1.4 V with aqueous electrolytes. This work suggests a micropore-forming strategy for the preferred porous carbon, which can be applied in supercapacitors, batteries, filters, adsorbents, and catalysts.

1. Introduction

Porous carbon, due to its large specific surface area (SSA), high stability, and surface chemistry, has been applied widely, especially in catalyst carriers, gas sorption and energy storage.[1] Supercapacitors, as a type of green energy storage device with high power density, excellent rate capability and ultralong cycle life, have been widely used in hybrid vehicles, power grids, and microelectronic products.[2] Porous carbon is by far the most widely used electrode material of supercapacitors due to its tunable pore structure, nice electrical conductivity, high specific surface area and good chemical/thermal stability.[3] The regular isolated or interconnected pores in porous carbon can be categorized into micropores (<2 nm), mesopores (2–50 nm), and macropores (>50 nm).[4] It was once adopted that the best strategy to increase capacitance was to maximize electrochemical double-layer charging,[5] and thus, the challenge at that time was to develop new mesoporous carbons with as high a specific surface area as possible.[6] Later, a different, more efficient desolvation mechanism was discovered in submicropores (<1 nm),[7] which could endow the porous carbon higher capacitance, larger density, wider voltage window and lower self-discharge. However, too small pore size (<0.5 nm, less than the twice of the ion size) causes the dense ion layers of adjacent pore walls to impinge on each other, reducing the surface area available for double-layer formation, hindering ion diffusion, and resulting in a tardy kinetics, which is unfavorable for a high mass-loading.[8] Therefore, how to precisely regulate the pore size of porous carbon is a key factor for realizing high-performance supercapacitors. Constructing porous carbon of sub-nanometer pores (0.5–1.0 nm) are expected to realize high capacitance, wide voltage window, low self-discharge and high mass-loading in the meantime, that has never been reported yet.

The conventional carbonization-activation routes for porous carbon cannot control the pore structures precisely, resulting in wide pore size distributions from several to 100 nm.[9] To overcome these problems, various templates have been employed to fabricate porous carbon with specific structural features, which can be categorized to hard templates, soft templates and self-templates, respectively. The hard template methods are able to precisely manipulate the porous structures, but the construction and removal of these templates such as SiO_2, ZnO, and MgO are cumbersome and laborious, and the obtained structures are mainly macroporous and mesoporous.[10] On the contrary, the soft template methods employ small organic molecules, surfactants, and copolymers to construct porous structures, and these templates are easy to remove by washing or calcination. But the processes of removing templates often cause the structure to collapse, and many popular soft templates are too expensive for the

X.-R. Zhang, T.-B. Song, T.-L. He, Q.-L. Ma, Z.-F. Wu, Y.-G. Wang, H.-M. Xiong
Department of Chemistry and Shanghai Key Laboratory of Molecular Catalysis and Innovative Materials
Fudan University
Shanghai 200438, P. R. China
E-mail: ygwang@fudan.edu.cn; hmxiong@fudan.edu.cn

The ORCID identification number(s) for the author(s) of this article can be found under https://doi.org/10.1002/adfm.202419219

DOI: 10.1002/adfm.202419219

 © 2024 Wiley-VCH GmbH

16163028, 2025, 16, Downloaded from https://advanced.onlinelibrary.wiley.com/doi/10.1002/adfm.202419219 by Fudan University, Wiley Online Library on [23/04/2025]. See the Terms and Conditions (https://onlinelibrary.wiley.com/terms-and-conditions) on Wiley Online Library for rules of use; OA articles are governed by the applicable Creative Commons License

large-scale production.[11] Different from the above two methods, self-template methods utilize self-containing species as templates to produce pores, and thus the templates become the composition of the final products. A classic example is the activated carbon made from biomass, owning large specific surface areas and low prices in the market.[12] However, their porous structures are difficult to control precisely to meet the ever-growing requirements of electrochemical supercapacitors, including adjustable hierarchical pores, additional pseudocapacitance, high wettability and multi-element doping states. Particularly, all the above template methods cannot produce porous carbon with dominant sub-nanometer pores (0.5–1.0 nm) that are essential for electrochemical supercapacitors. Therefore, developing an all-in-one self-template method to produce porous carbon electrodes for supercapacitors remains a huge challenge at present.

Carbon dots (CDs), especially the carbonized polymer dots (CPDs), are a class of novel carbon nanomaterials, whose structures are between inorganic nanocrystals (hard templates) and organic polymer dots (soft templates).[13] When used as templates, CDs will bring about outstanding performance in fabricating porous carbon. On one hand, CDs have good solubility in various solvents, which can be dispersed homogeneously in the matrix to produce uniform pores. On the other, the controllable compositions of CDs endow them the ability to dope heteroatoms into the matrix, and graft functional groups on the matrix surfaces.[14] It is amazing that although possessing both merits of hard templates and soft templates simultaneously, the well-designed CDs are intrinsically self-templates for producing porous carbon. In the present work, we prepared N-doped CDs (NCDs) and PEGDGE-DETA composite hydrogels (named as NCD@PDHs) by the amine-epoxy ring-opening reaction, and then fabricate carbonized PDHs (named as CPDHs) by thermal treatment, in which NCDs act as the self-templates. The decomposition of CDs during carbonization and activation resulted in the preferred sub-nanometer pores (0.64–0.80 nm), doped elements, and functionalized channel surfaces. As a result, the assembled symmetric supercapacitors (SSCs) show high energy density, low self-discharge, and excellent cycling stability in a wide voltage range of 1.4 V with a high mass-loading (10 mg cm^{-2}) of each single-electrode.

2. Results and Discussion

The preparation process of such unique carbon material is shown in **Scheme 1**, where CDs play as crosslinkers, pore-forming agents, and N dopants in the meantime, and diethylenetriamine (DETA) is used to maintain the hydrogel structure as an additional cross-linker. The intrinsic pore-forming mechanism was investigated by setting up a control group (named as PDH) adding only poly(ethylene glycol) diglycidyl ether (PEGDGE) and DETA and a control group (named as NCD@PH) adding only CDs and PEGDGE. First, NCDs were synthesized through a hydrothermal reaction of citric acid (CA) and DETA at 170 °C for 5 h. Second, an amine-epoxy ring-opening polymerization reaction between the amino groups of NCDs and PEGDGE was carried out at 80 °C, resulting in a self-assembled hydrogel network. Subsequently, the obtained NCD@PDH hydrogel was treated with an aqueous KOH solution at 90 °C for 12 h to disrupt the amide bonds in NCDs, leading to the formation of pores and carbon fragments that would develop into sub-nanometer pores during the subsequent calcination. Notably, the binding sites between NCDs and the polymer chains remained intact during the alkali treatment, allowing the NCDs fragments to serve as N dopants within the polymer network. Before this treatment, DETA was introduced to preserve the hydrogel's mechanical structure after NCDs cleavage, as NCD@PH hydrogel without DETA would rapidly collapse and decompose under alkaline conditions (Figure S1, Supporting Information). Finally, the alkali-treated hydrogel was washed, dried, and calcined with $ZnCl_2$ under a N_2 atmosphere, yielding hierarchically porous carbon (CPDH-x, where x represents the amount of NCDs added). In this way, the pore sizes and specific surface areas of the final products were adjusted by changing the content of NCDs during hydrogel preparation successfully. And the NCDs play as both self-templates for producing sub-nanometer pores and N-dopants for modifying channels in the whole process.

Transmission electron microscopy (TEM) and high-resolution TEM (HRTEM) were employed to study our NCDs. **Figure 1a** and Figure S2 (Supporting Information) show that NCDs are monodispersed with a predominant diameter of 3–5 nm, while Figure 1b shows a distinct lattice fringe spacing of 0.21 nm, consistent with the (100) plane of graphite.[15] The XRD pattern in Figure 1c shows the typical diffraction of CDs at ≈23.5°, where the broad diffraction peak confirms the nano size and low crystallinity of NCDs.[16] In Figure 1d, the FTIR vibration bands at ≈3438, 2838–3000, 1550–1650, 1360, and 1104 cm^{-1} correspond to the O—H/N—H, C—H, C═O/C═N, C—N and C—O groups, respectively. This result confirms that the NCDs contain a large number of amide bonds and amine groups. These amide bonds can be cut off by KOH etching, and thus the MALDI-TOF MS of the sample before and after etching shows the significant decrease of the molecular weights from 700–900 to 500–650 Da (Figure 1e). This phenomenon suggests that NCDs are stripped into small pieces by KOH due to the disintegration of amide bonds. As a result, the typical blue fluorescence of NCDs decays after KOH etching (Figure 1f).

The HRTEM images of PDH (**Figure 2a**) show the sample is a solid hydrogel with no porous structure after KOH etching (Figure 2b). In contrast, the sample NCD@PDH-0.4 has many NCDs (Figure 2c), which change to be numerous pores after KOH etching (Figure 2d). It is worth noting that due to the difficulty in observing individual NCDs, the circled area in Figure 2c represents the aggregation of NCDs. In addition, the morphology and the chemical composition of NCD@PDH-0.4 are investigated by the scanning electron microscopy (SEM) and the energy dispersive spectrometer (EDS). Figure S3 (Supporting Information) shows C, N, and O elements are uniformly distributed in the hydrogel, implying a homogeneous distribution of NCDs. After calcination with $ZnCl_2$, PDH transforms into CPDH, which shows a coarse surface in SEM images (Figure 2e) and a stacked carbon structure in TEM images (Figure 2f). In contrast, the optimal sample CPDH-0.4 shows a honeycomb morphology in SEM images (Figure 2g) and plenty of channels in TEM images (Figure 2h). Such a porous structure increases both the reaction sites and the shuttling paths in the carbon electrodes, thus improving both the capacity and the rate performance of the supercapacitor effectively. In order to optimize the CPDH-x samples, different amounts of NCDs were added into the preparation

 © 2024 Wiley-VCH GmbH

16163028, 2025, 16, Downloaded from https://advanced.onlinelibrary.wiley.com/doi/10.1002/adfm.202419219 by Fudan University, Wiley Online Library on [23/04/2025]. See the Terms and Conditions (https://onlinelibrary.wiley.com/terms-and-conditions) on Wiley Online Library for rules of use; OA articles are governed by the applicable Creative Commons License

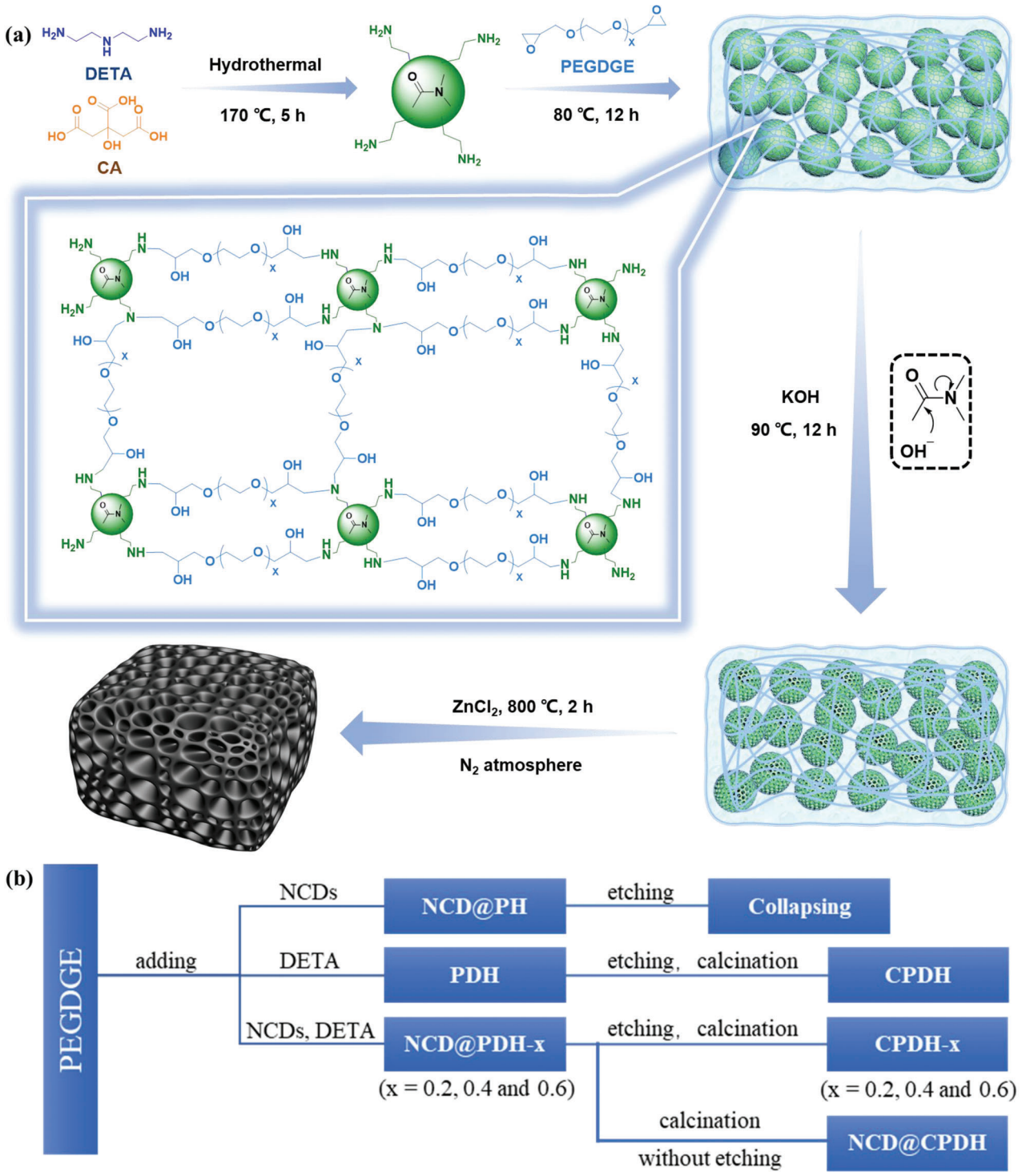

Scheme 1. a) Schematic diagram and b) flowchart of the synthetic procedure for CPDHs.

process respectively. CPDH-0.2 shows a channel structure but the pores are sparse and disordered (Figure S4a,b, Supporting Information), while CPDH-0.6 has a blocky shape with macropores of irregular sizes. (Figure S4c,d, Supporting Information). These phenomena indicate that less NCDs cannot generate a large number of pores uniformly, while more NCDs will aggregate in hydrogels which form irregular macropores. In order to figure out the pore-forming mechanism, a control sample without KOH etching is investigated, that NCD@CPDH shows a rough, dense surface and a tiered structure like CPDH (Figure S4e,f, Supporting Information), and thus the etching step is crucial for the pore-forming function of NCDs.

 © 2024 Wiley-VCH GmbH

16163028, 2025, 16, Downloaded from https://advanced.onlinelibrary.wiley.com/doi/10.1002/adfm.202419219 by Fudan University, Wiley Online Library on [23/04/2025]. See the Terms and Conditions (https://onlinelibrary.wiley.com/terms-and-conditions) on Wiley Online Library for rules of use; OA articles are governed by the applicable Creative Commons License

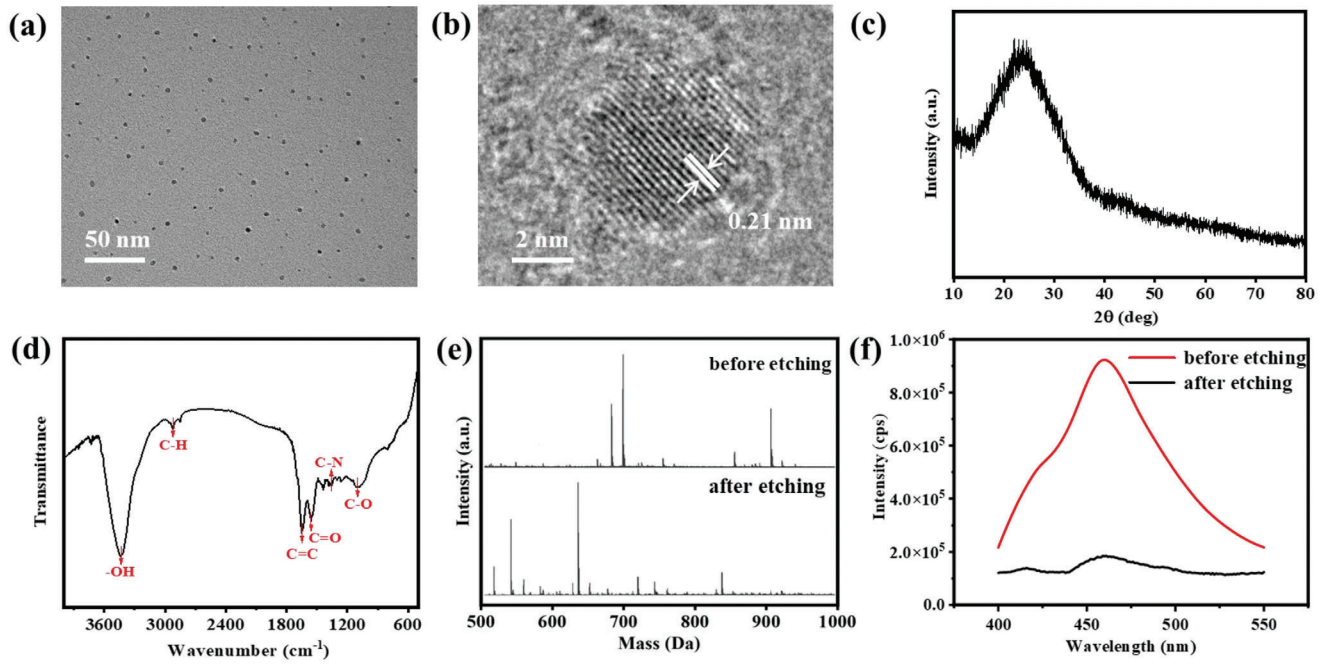

Figure 1. a) TEM image, b) HRTEM image, c) XRD pattern, and d) FTIR spectrum of NCDs. e) MALDI-TOF MS spectra and f) PL spectra of NCDs before and after KOH etching.

The pore size distribution curves (Figure 3a) based on the density flooding theory (DFT) method show that compared to CPDH and NCD@CPDH, similar abundant sub-nanometer pores (concentrated in 0.64–0.80 nm) are found in CPDH-0.2, CPDH-0.4 and CPDH-0.6, which match perfectly with the ion size,[7,17] confirming the reproducibility of this method. Notably, NCD@CPDH owns fewer micropores which mainly distributed within 0.8–2 nm, further illustrating the key role of KOH etching on NCDs in the formation of sub-nanometer pores. And pores smaller than 1 nm are not observed in CPDH, which excludes the possibility that sub-nanometer pores were introduced merely from KOH, corroborating the unique role of CDs as self-templates. The nitrogen adsorption-desorption isotherms of all samples are also compared in Figure S5 (Supporting Information), which display H4-type hysteresis loops at relative pressures of 0.4–1.0, implying the dominance of narrow slit-pores in the porous carbon. To clarify the role of $ZnCl_2$ in the activation process, the porous carbon performance of CPDH-0.4 without $ZnCl_2$ activation was added for comparison (Figure S6, Supporting Information). The comparison with NCD@CPDH in Figure 2a leads to the conclusion that the formation of the pore size distribution is not reliant on $ZnCl_2$ activation but rather on the etching step, while $ZnCl_2$ serves to enhance the etching effect. Table S1 (Supporting Information) confirms that the introduction of NCDs in the precursor hydrogels had a significant effect on the S_{BET} and the pore size distribution of final products, among which CPDH-0.4 has an S_{BET} of 1020.4 $m^2\ g^{-1}$ and a V_{tot} of 0.632 $cm^3\ g^{-1}$, much higher than the other samples (Figure 3b,c). The mesopores play as fast channels for ion migration, and the sub-nanometer pores provide abundant adsorption sites for desolvated ions.[18] Pores smaller than 0.5 nm (Figure 3d) hold an ultra-high desolvation effect and K^+ ions can be confined in monolayer, but this implies low utilization of adjacent pore wall space and that ions have difficulty diffusing into these pores.[19] Within the range of pores from 0.5 to 1 nm (Figure 3e), a high desolvation effect still reamins, bringing K^+ ions closer to the electrode surface while leaving enough space to provide rapid ion transport.[20] Desolvation effect hardly takes place at pore size larger than 1 nm (Figure 3f), which means high over-screening effect, resulting in double-layer loss.[21] To further elucidate the effect of different pore sizes on K^+ ion transport, the dynamic interaction energies of K^+ ion diffusion from infinity to the center of pores are obtained through density functional theory (DFT) calculations, using optimized structures of K^+ ion adsorbed on double-layer graphene with layer distances of 0.4, 0.6, 0.8, 1.0 and 1.2 nm (Figure 3g). Obviously, decreasing from 1.2 nm, the smaller the pore size, the more favorable the entry of K^+ ions. However, when it comes to pores with a diameter of 0.4 nm, a high energy barrier emerges, indicating unfavorable entry processes. As a result, the sub-nanometer pores (0.64–0.80 nm) in CPDHs promotes a synergistic enhancement in capacitance and charging dynamics.

The X-ray diffraction (XRD) patterns in Figure S7a (Supporting Information) show that CPDHs have two diffraction peaks at ≈24° and 44°, corresponding to the (002) and (100) planes of the graphitic structure respectively, while the broad peak widths indicate the crystallinity of the carbon structure is low.[22] Raman spectra of these samples are compared in Figure S7b (Supporting Information), which show the typical D bands at 1343 cm^{-1} and the G bands at 1595 cm^{-1}, respectively. D bands are attributed to the disordered sp^3 carbon or defect-induced mode, while G bands are associated with sp^2-hybridized carbon (vibration with $E_{2\ g}$ symmetry).[23] Besides, weak and broad 2D bands can be seen near 2870 cm^{-1}, which verifies the existence of

 © 2024 Wiley-VCH GmbH

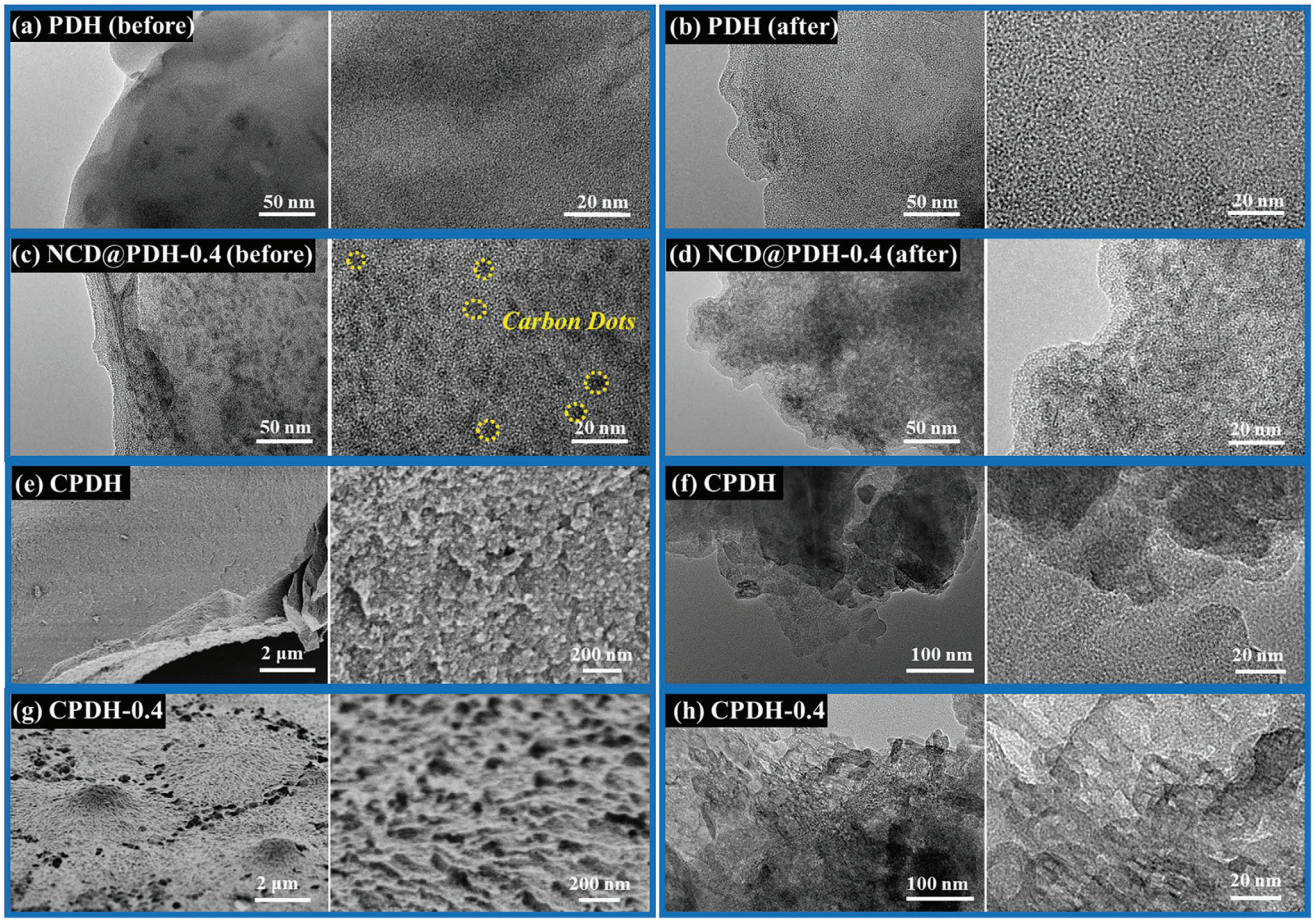

Figure 2. HRTEM images of a,b) PDH and c,d) NCD@PDH-0.4 before and after KOH etching, respectively. SEM and HRTEM images of e,f) CPDH and g,h) CPDH-0.4, respectively.

multilayered graphene-like sheets.[24] The intensity ratio of D to G bands (I_D/I_G) is commonly used to estimate the degree of graphitization of carbon structures.[25] It is clear that the I_D/I_G peak intensity ratio of CPDH-x increases along with the x value, to the maximum when x = 0.4. This means the defects in the final products are enhanced by NCDs incorporation, which will benefit the electrochemical performance of the porous carbon.

Fourier Transform Infrared Spectrometer (FTIR) spectra show that all porous carbon samples contain abundant amounts of —OH, C—O—C, and C—N functional groups, which provide good wettability and additional capacity for the electrode materials (Figure S8, Supporting Information). X-ray photoelectron spectroscopy (XPS) analyses further confirm that the introduction of NCDs increases the contents of N and O (Table S2, Supporting Information). Each element of all samples (Figure S9a–f, Supporting Information) was investigated, respectively. All porous carbons possess high oxygen contents due to the abundant oxygen-containing groups in the precursors, which generally favor the hydrophilic and pseudocapacitive properties of the materials.[26] NCDs are rich in N and O functional groups, and their incorporation directly increases the proportion of N and O elements in the system. During the etching process, however, the amide structures, which are critical sources of N and O, are disrupted, resulting in the fragmentation of NCDs. This transformation generates carboxyl and amino groups, which are more easily removed during the calcination process. Consequently, NCD@CPDH samples that have not undergone etching exhibit the highest N and O content. Compared with CPDH, the C 1s spectrum of CPDH-0.4 shows the sample has a higher C-N content due to the N-doping effect of NCDs. The appropriate amount of N doping not only improves the wettability of the electrodes, but also optimizes the electronic structure and charge transfer kinetics. The N 1s region can be deconvoluted into four main peaks at 398.4, 400.3, 401.4, and 402.5 eV, corresponding to N-6 (pyridine N), N-5 (pyrrole N), N-Q (quaternary N), and N-X (N-oxidation) species, respectively. Among them, both N-6 and N-5 are the main contributors to the pseudocapacitance and the potential window up to 1.4 V.[27] N-6 provides a lone pair of electrons to the π-system, serving as electron-donor in the graphitic layer, while N-5 provides two p-electrons to the π-system.[28] Comparing CPDH and CPDH-0.4 in Table S3 (Supporting Information), the introduction of NCDs has increased the proportions of N-6 and N-5 from 32% to 49% and from 25% to 30%, respectively. The similar conditions are also observed in CPDH-0.2 and CPDH-0.6. In brief, both FTIR and XPS analyses confirm that CPDHs have good wettability and conductivity based on their hierarchical porous,

© 2024 Wiley-VCH GmbH

16163028, 2025, 16, Downloaded from https://advanced.onlinelibrary.wiley.com/doi/10.1002/adfm.202419219 by Fudan University, Wiley Online Library on [23/04/2025]. See the Terms and Conditions (https://onlinelibrary.wiley.com/terms-and-conditions) on Wiley Online Library for rules of use; OA articles are governed by the applicable Creative Commons License

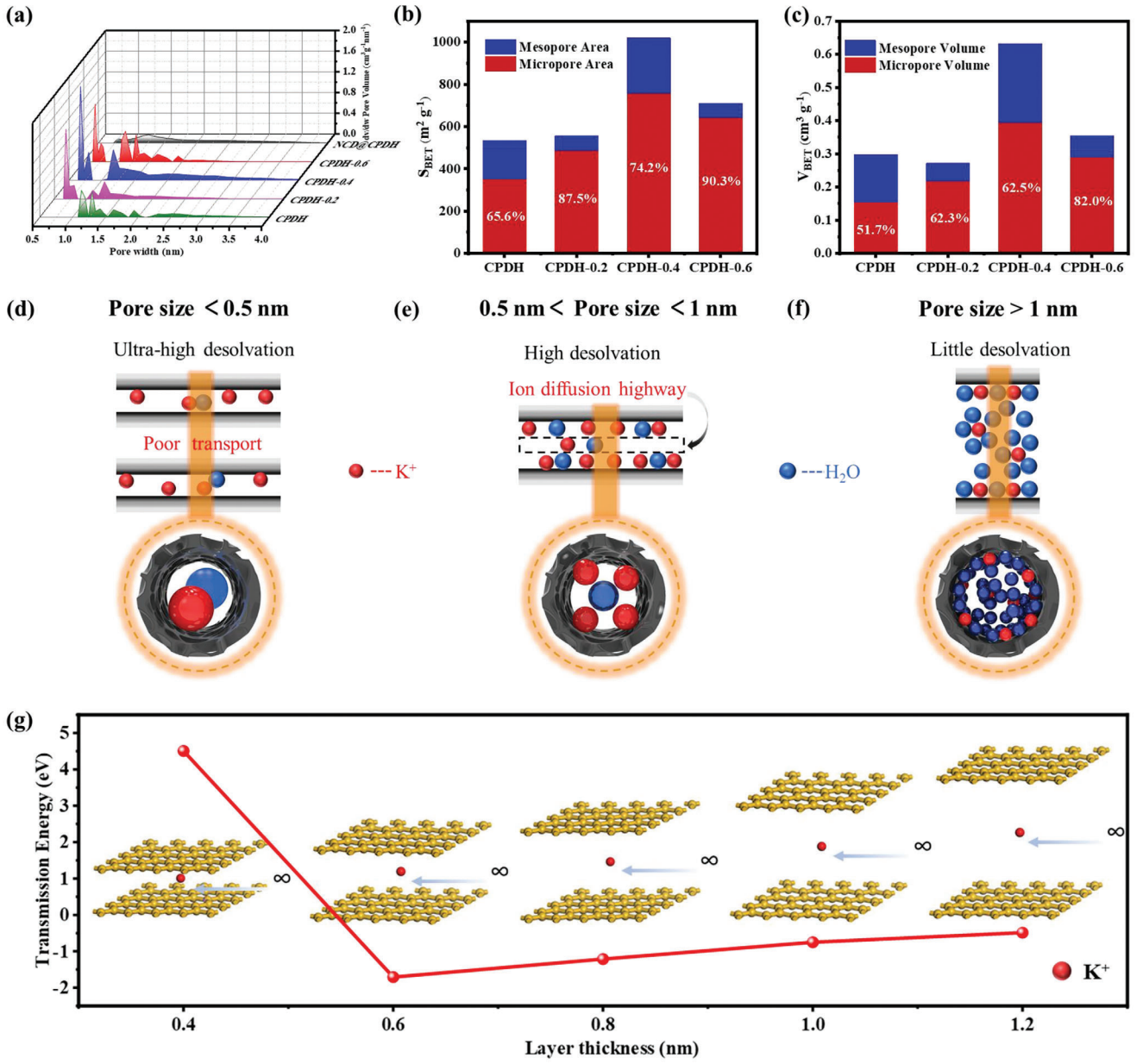

Figure 3. a) Pore size distributions calculated by the DFT method. b) Specific surface areas and c) specific pore volumes of different samples measured by BET methods. Schematics of K^+ ions residing in pores with sizes: d) smaller than 0.5 nm, e) between 0.5 and 1 nm (sub-nanometer pore), and f) larger than 1 nm. g) DFT simulations of K^+ ion diffusion from infinity to the center of pores.

surface hydrophilic and nitrogen-oxygen co-doped structures, which endow CPDHs promising application in supercapacitors.

Electrochemical tests on CPDHs in terms of CV (cyclic voltammetry), GCD (galvanostatic charge/discharge), and EIS (electrochemical impedance spectroscopy) are carried out respectively in a three-electrode system with 6 m of KOH aqueous electrolyte (**Figure** 4a–e; Figures S10–S12, Supporting Information). At first, the CPDHs performance is studied with a low mass-loading of 1 mg cm^{-2}. At a scan rate of 50 mV s^{-1}, all shapes of CV curves are quasi-rectangular with a weak reversible hump (Figure 4a), that is a typical EDLC (electric double layer capacitor) behavior, containing a few pseudocapacitance, closely related to the reversible redox reactions of oxygen/nitrogen functional groups.[26a,29] In an alkaline media, the hydrophilicity of oxygen-containing functional groups promotes the insertion/de-insertion of hydrated ions into the porous structure to contribute to the pseudo-capacitance, whereas the highly electronegative N promotes the adsorption of electrolyte ions and acts as an electron donor.[28b,30] Among these samples, CPDH-0.4 has the largest CV integral area, which means the best charge storage capacity, in accord with its high S_{BET} and abundant sub-nanometer pores. The GCD curves at a current density of 1 A g^{-1} for each sample are displayed in Figure 4b, where all curves are isosceles triangular with the negligible IR drop (-4 mV). Based on GCD curves, the

© 2024 Wiley-VCH GmbH

16163028, 2025, 16, Downloaded from https://advanced.onlinelibrary.wiley.com/doi/10.1002/adfm.202419219 by Fudan University, Wiley Online Library on [23/04/2025]. See the Terms and Conditions (https://onlinelibrary.wiley.com/terms-and-conditions) on Wiley Online Library for rules of use; OA articles are governed by the applicable Creative Commons License

16163028, 2025, 16, Downloaded from https://advanced.onlinelibrary.wiley.com/doi/10.1002/adfm.202419219 by Fudan University, Wiley Online Library on [23/04/2025]. See the Terms and Conditions (https://onlinelibrary.wiley.com/terms-and-conditions) on Wiley Online Library for rules of use; OA articles are governed by the applicable Creative Commons License

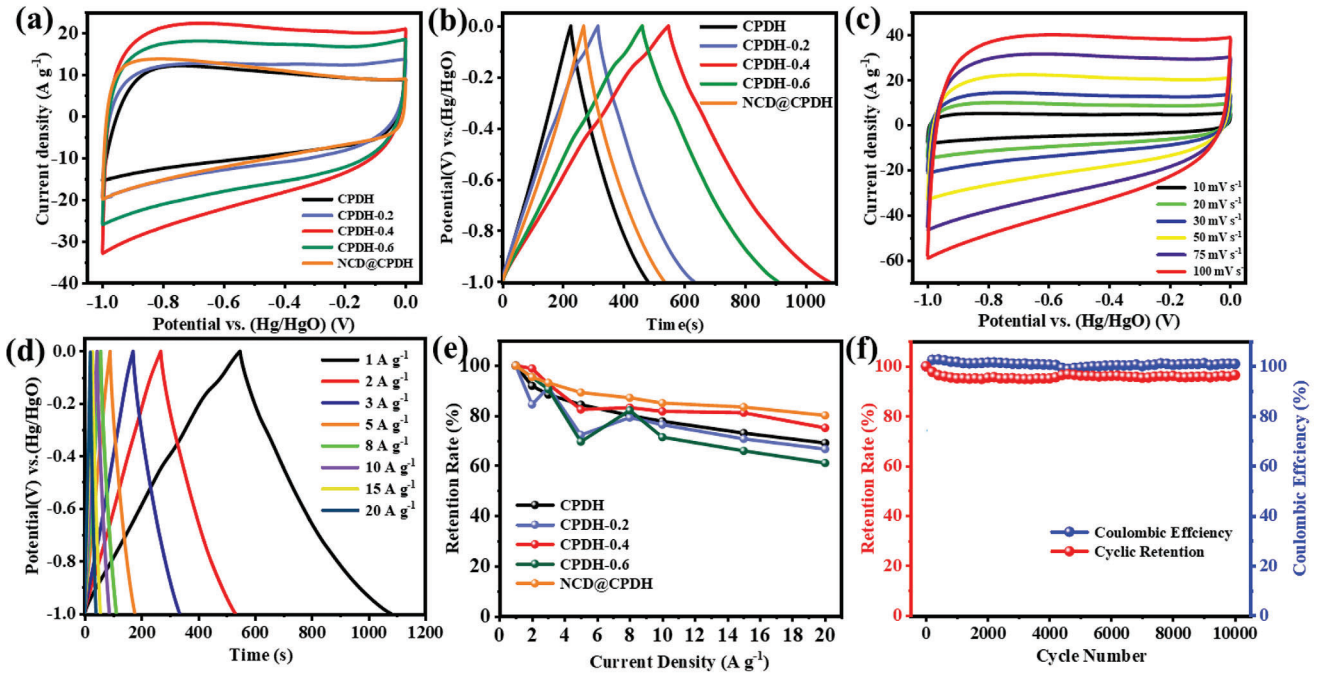

Figure 4. Electrochemical performances of CPDH and CPDHs (1 mg cm^{-2}) tested via a three-electrode system: a) CV curves at scan rates of 50 mV s^{-1}. b) GCD curves at 1 A g^{-1}. c) CV curves of CPDH-0.4 at various scan rates. d) GCD curves of CPDH-0.4 at various current densities. e) The rate performance of different samples at various current densities. f) Cycling stability and coulombic efficiencies of CPDH-0.4 for 10000 cycles at 5 A g^{-1}.

gravimetric specific capacitances of all the electrodes are calculated at 1 A g^{-1}. The CPDH-0.4 electrode exhibited the highest gravimetric specific capacitance of 531 F g^{-1}, while the specific capacitances of the CPDH, CPDH-0.2, CPDH-0.6, and NCD@CPDH electrodes are 255, 318, 448 and 266 F g^{-1}, respectively. The CV curves of the CPDH-0.4 electrode and others are measured at different scan rates (Figure 4c; Figure S10, Supporting Information), while its GCD curves were recorded at different current densities (Figure 4d; Figure S11, Supporting Information). The rectangular CV curves at high scan rates and the symmetric GCD curves at high current densities indicate the reversibility and high efficiency of the ion adsorption/desorption process, which means its capacitive superiority.[31]

To further compare the energy storage capacity of all samples, their capacitance retention at different current densities is shown in Figure 4e, in which NCD@CPDH has the best rate performance due to its highest N doping content.[32] In Figure 4f, CPDH-0.4 maintains 96.7% of the original capacitance, and exhibits nearly 100% of the coulombic efficiency after 10000 cycles at 5 A g^{-1}, demonstrating its excellent cycling stability. The typical performance parameters of CPDH-0.4 are compared with other low mass-loading porous carbon materials in literature (Table S4, Supporting Information), which further validates the advantages of our present work. The ion diffusion and transport kinetics of electrolytes in these samples are further analyzed using EIS analysis. As shown in Figure S12a (Supporting Information), all the Nyquist plots present steeper linear curves corresponding to the ideal capacitance in the low frequency region and show semicircles corresponding to the internal/surface resistance in the high frequency region. Table S5 (Supporting Information) shows that the introduction of NCDs significantly reduces the intrinsic resistance (R_s) and charge transfer resistance (R_{ct}) of CPDHs. In the Bode plot (Figure S12b, Supporting Information), all samples have low frequencies close to the phase angle of –90°, which are the typical capacitive features. In addition, the characteristic relaxation time τ_0 calculated from f_0 (the frequency at half of the maximum capacitance value) for CPDH, CPDH-0.2, CPDH-0.4, and CPDH-0.6 are 5.6, 2.6, 6.7 and 6.7 s, respectively, demonstrating the fast charge/discharge performance.[33]

To test the high loading performance of the material, the optimal sample of CPDH-0.4 is improved to 10 mg cm^{-2}, and its specific capacitance decreases to 515.5 F g^{-1} at a current density of 1 A g^{-1}, owing to the insufficient ion diffusion in the electrode materials. The capacitance ineluctably decreases as the current density increases gradually, because the filling amount of electrolyte ions in the sub-nanometer pores decreases when the charge shuttle speed increases. As a result, the capacitance of CPDH-0.4 drops to 403.7 F g^{-1} at 10 A g^{-1}. Nevertheless, the capacitance retention of 78.3% is an excellent rate performance, due to the indispensable part of meso- and macropores which can accelerate the transfer of electrolyte ions to the sub-nanometer pores (Figure S13a–c, Supporting Information). The higher mass-loading of electrode material leads to the higher areal capacitance, and thus, CPDH-0.4 exhibits a high areal specific capacitance of 5.16 F cm^{-2} at 1 A g^{-1} and 4.04 F cm^{-2} at 10 A g^{-1} at the high mass-loading of 10 mg cm^{-2}. The volumetric specific capacitance depends not only on the structure of the electrode material, but especially on its packing density. Owing to the limited microporous surface area (S_{micro}/S_{total}>70%), CPDH-0.4 has a high packing density (0.81 g cm^{-3}), possessing the high

 © 2024 Wiley-VCH GmbH

16163028, 2025, 16, Downloaded from https://advanced.onlinelibrary.wiley.com/doi/10.1002/adfm.202419219 by Fudan University, Wiley Online Library on [23/04/2025]. See the Terms and Conditions (https://onlinelibrary.wiley.com/terms-and-conditions) on Wiley Online Library for rules of use; OA articles are governed by the applicable Creative Commons License

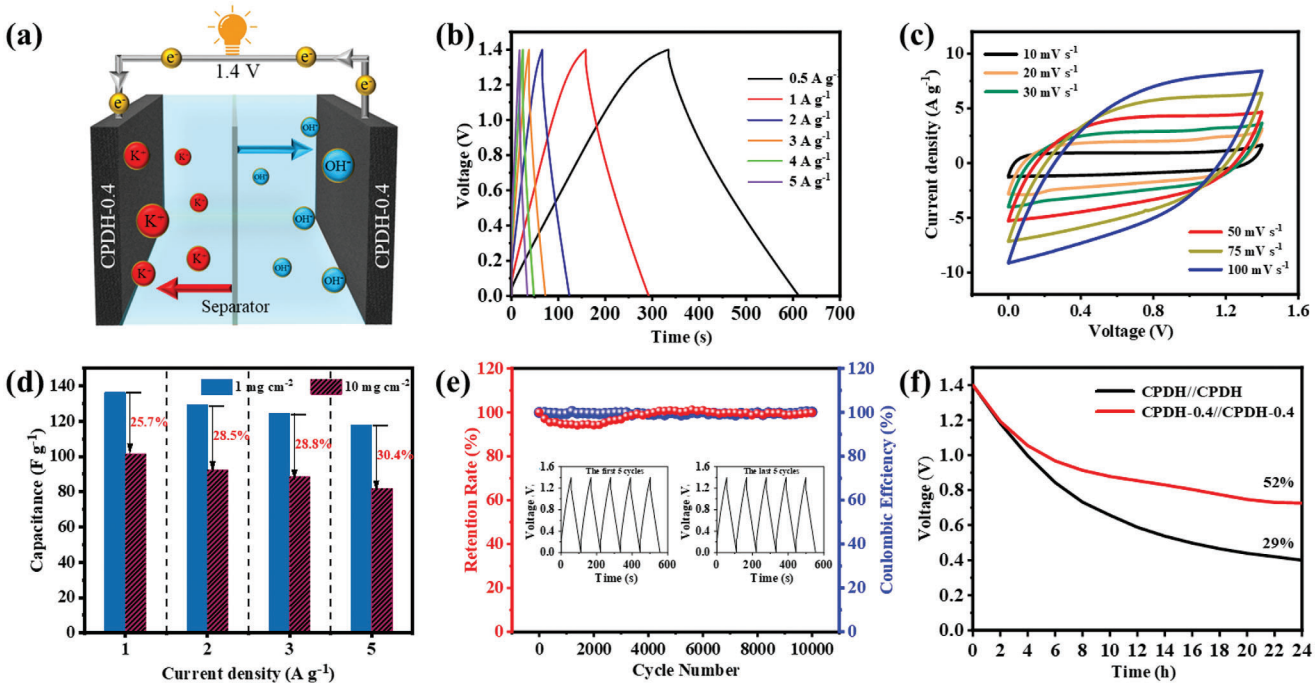

Figure 5. Electrochemical performances of CPDH-0.4//CPDH-0.4 symmetric supercapacitors (with single-electrode mass-loading of 10 mg cm^{-2}) in 6 m of KOH electrolyte: a) Schematics illustration of the symmetrical supercapacitor device. b) GCD curves at various current densities. c) CV curves at various scan rates. d) Comparison of specific capacitance between single-electrode mass-loading of 1 and 10 mg cm^{-2}. e) Cycling stability at 2 A g^{-1} after 10000 cycles. (Insets are the GCD curves of the first and last five cycles.) f) Self-discharge curves of symmetric supercapacitors.

volumetric specific capacitance of 417.6 F cm^{-3} at 1 A g^{-1} and 327.0 F cm^{-3} at 10 A g^{-1}, respectively. The capacitance parameters of CPDH-0.4 are compared with other high mass-loading porous carbon materials in Table S6 (Supporting Information), which verifies its outstanding advantage in high mass-loading. A deviation from rectangle of CV curve is observed due to the stronger polarization of the higher mass-loading electrode (Figure S13b, Supporting Information). When the mass-loading reaches 10 mg cm^{-2}, R_s is 0.62 Ω and the relaxation time constant τ_0 is 15.6 s (Figure S13d,e, Supporting Information). This suggests that, despite of the electrode thickening, the charge storage and the ion mobility kinetics are not inhibited significantly. Similarly, GCD tests of 10 000 cycles are performed at 5 A g^{-1}, which show the capacitance retention of 95.7% and the coulombic efficiency of 100% (Figure S13f, Supporting Information), almost the same with its performance at 1 mg cm^{-2} (Figure 4f).

A symmetric supercapacitor using CPDH-0.4 electrodes (1 mg cm^{-2}) is first fabricated and 6 m of KOH aqueous solution as the electrolyte (**Figure 5a**), and its CV curves at 50 mV s^{-1} in the voltage range of 0–1.5 V are shown in Figure S14a (Supporting Information). Obviously, even if the operating voltage is increased to 1.4 V, the CV curves present an ideal quasi-rectangle with no large anode current peak.[34] And the operating voltage of SSCs is set at 1.4 V to measure CV data with various scan rates, which exhibit a good rate performance even when the scan rate is increased to 150 mV s^{-1}. The GCD curves of SSCs under different current densities are all symmetrical triangles (Figure S14b, Supporting Information), confirming their ideal electrochemical reversibility and Coulomb efficiency. According to the GCD curves, the specific capacitances of SSCs at different current densities are present in Figure S14c (Supporting Information), 136.3 F g^{-1} at 1 A g^{-1} and 109.7 F g^{-1} at 10 A g^{-1} respectively. As shown in Figure S14d (Supporting Information), the voltage window does not show a large redox peak until it broadens to 1.5 V, presumably because the large number of sub-nanopores inhibited the entry of water molecules into the pores, thus reducing their electrochemical decomposition. The Nyquist plots (Figure S14e, Supporting Information) displays that the high frequency region and low frequency regions have a little semicircle and a nearly vertical line, respectively, representing the excellent charge transfer dynamics and EDLC properties of SSCs. The Bode plot (Figure S14f, Supporting Information) shows a characteristic frequency f_0 of 0.28 Hz, corresponding to a time constant τ_0 of 3.6 s, which means its fast charge-discharge rate. Finally, the cycling life of SSCs in the 6 m of KOH electrolyte are evaluated by GCD tests. As shown in Figure S15a (Supporting Information), the retention rate increases at the first few hundred cycles, and the specific capacitance of SSCs can still maintain 100% of the initial value after 10000 cycles, while the Nyquist plot only changes slightly in comparison with the initial one (Figure S15b, Supporting Information), indicating an excellent electrochemical cycle stability. The energy and power densities are 37–30 Wh kg^{-1} and 700–7000 W kg^{-1}, respectively, which are competitive in comparison with other reported carbon materials using KOH electrolytes (Figure S16, Supporting Information).

When the SSCs are fabricated by CPDH-0.4 electrodes (10 mg cm^{-2}), the GCD curves under different current densities still remains symmetrical triangles (Figure 5b) and the CV curves maintain a quasi-rectangle shape up to 100 mV s^{-1} with no

 © 2024 Wiley-VCH GmbH

16163028, 2025, 16, Downloaded from https://advanced.onlinelibrary.wiley.com/doi/10.1002/adfm.202419219 by Fudan University, Wiley Online Library on [23/04/2025]. See the Terms and Conditions (https://onlinelibrary.wiley.com/terms-and-conditions) on Wiley Online Library for rules of use; OA articles are governed by the applicable Creative Commons License

large anode current peak (Figure 5c). The specific capacitance decreases to 101.3 F g^{-1} at a current density of 1 A g^{-1} and drops to 82.0 F g^{-1} at 5 A g^{-1} and the retention of 80.9% shows the excellent rate performance (Figure 5d). What's more, the loss of capacity is only ≈25%-30% when the mass loading is multiplied by 10 times, which further illustrates the high mass-loading performance. The device displays 99.9% of capacitance retention after 10000 cycles and consistently maintains 100% Coulombic efficiency (Figure 5e). When the single-electrode mass-loading reaches 10 mg cm^{-2}, R_s is 1.43 Ω and the relaxation time constant τ_0 is 9.4 s, respectively (Figure S17, Supporting Information). The equivalent circuit in Figure S18 (Supporting Information) is used to fit all Nyquist spectra using the software ZVIEW. The energy density of the SSCs is 27.8 Wh kg^{-1} at 350 W kg^{-1} and 22.3 Wh kg^{-1} at 3500 W kg^{-1}, respectively. Finally, the SSCs are charged to 1.4 V and then their self-discharge curves are recorded within 24 h (Figure 5f). CPDH-0.4//CPDH-0.4 shows an obvious voltage drop of 0.35 V at the first 4 h, and a slow voltage drop of 0.33 V during the next 20 h, resulting in a final voltage retention of 52%. The open circuit voltage potential of CPDH//CPDH declines rapidly, and the final retention rate after 24 hours is only 29%. Therefore, the sub-nanometer pores formed by NCDs can not only increase the capacitance, but also restrain the desorption rate of ions effectively, thus mitigating the self-discharge of supercapacitors.

3. Conclusion

We developed a hydrogel composite material with CDs as crosslinking agent, pore-forming agent, and dopant, and used it as a precursor to prepare porous carbon for supercapacitors. The NCDs self-template was first evenly dispersed into the main structure of the hydrogel by chemical crosslinking process, and then the template is removed by simple alkali washing to form a porous hydrogel while N atoms were doped in the skeleton. The porous carbon produced from this precursor did not have to worry about the problem of template residue, and displayed a hierarchical porous structure rich in sub-nanometer pores (0.64–0.80 nm). Benefiting from the particular pore structure, the symmetric supercapacitor based on the high mass-loading CPDH-0.4 electrodes delivers a high energy density of 22.3 Wh kg^{-1} at 3500 W kg^{-1}, respectively), showing wide voltage window, low self-discharge and excellent high mass-loading performance. CDs as a new series of nanoscale organic self-templates enable materials to obtain larger specific surface areas, abundant sub-nanometer pores and designable element doping, which has great potential application in the field of porous carbon manufacturing process.

4. Experimental Section

Synthesis of Nitrogen-Doped Carbon Dots (NCDs): 1.5 g of CA and 0.9 mL of DETA were dissolved in 10 mL of water, and then transferred into a Teflon-lined stainless-steel autoclave. The autoclave was heated at 170 °C for 5 h. After cooling to room temperature, the CDs solution was purified by dialysis through a 1500 MW cut off membrane. The solution was then freeze-dried to obtain yellow powder NCDs.

Synthesis of NCD@PEGDGE-DETA Hydrogels (NCD@PDHs): 2.4 g of PEGDGE and 0.08 mL of DETA were dissolved in 3.92 mL of water, followed by adding different amounts (0, 0.2, 0.4, 0.6 g) of NCDs, respectively. The obtained homogeneous solutions were heated in an 80 °C oil bath for 12 h until the solutions turned into hydrogels. These hydrogels were named as PDH or NCD@PDH-x, in which x (x = 0.2, 0.4, and 0.6) represents the amount of NCDs added (For PDH, x = 0).

Synthesis of Carbonized Hydrogels: (CPDHs and NCD@CPDH): The previous hydrogels were dried in vacuum to remove any adsorbed water and then put into 1 m of KOH aqueous solution at 90 °C for 12 h. Thereafter, the hydrogels were washed by water repeatedly and dried in a vacuum again, and then immersed into a $ZnCl_2$ solution for swelling. The mass ratio of the hydrogel and $ZnCl_2$ was 1:1. After absorption of all solutions, the composites were freeze-dried. The dried samples were heated in a tube furnace from room temperature to 300 °C at a speed of 5 °C min^{-1}, and then kept at 300 °C for 1 h. After that, the temperature was increased to 800 °C at 2 °C min^{-1} and kept at 800 °C for 2 h. After cooling down naturally to the room temperature, the resulting black powder was first washed by a 2 m of HCl aqueous solution and then washed by deionized water and ethanol respectively for several times. Finally, the products were dried at 80 °C overnight in a vacuum oven. The as-prepared carbonized hydrogel samples were signified as CPDH (x = 0) and CPDH-x (x = 0.2, 0.4 and 0.6), respectively. For comparison, another carbonized sample made from NCD@PDH-0.4 hydrogel without KOH treatment was obtained, named as NCD@CPDH.

Synthesis of NCD@PEGDGE Hydrogel (NCD@PH): 2.4 g of PEGDGE and 0.8 g of NCDs were dissolved in 4 mL of water, and then heated at 80 °C for 12 h to form hydrogel. The hydrogel was dried in vacuum to remove the adsorbed water and then put into 1 м of KOH aqueous solution with an oil bath at 90 °C, where it rapidly decomposed within 6 h.

Supporting Information

Supporting Information is available from the Wiley Online Library or from the author.

Acknowledgements

This study was financially supported by the National Natural Science Foundation of China (No. U24A20565, No. 21975048) and the Science and Technology Commission of Shanghai Municipality (No. 2024ZDSYS02).

Conflict of Interest

The authors declare no conflict of interest.

Data Availability Statement

The data that support the findings of this study are available from the corresponding author upon reasonable request.

Keywords

carbon dots, porous carbon, self-template, sub-nanometer pore, supercapacitors

Received: October 11, 2024
Revised: November 28, 2024
Published online: December 26, 2024

[1] a) J. X. Li, Y. L. Xu, P. Z. Li, A. Voelkel, F. I. Saldaña, M. Antonietti, N. López-Salas, M. Odziomek, *Adv. Mater.* **2024**, *36*, 2311655; b) J.

 © 2024 Wiley-VCH GmbH

L. Huang, Y. Q. Chen, Z. H. Cen, T. Yi, M. Liang, Y. L. Zhu, R. L. Liu, R. W. Fu, S. H. Liu, D. C. Wu, *Adv. Mater.* **2024**, *36*, 2403033; c) J. H. Lee, N. D. Loh, Z. Y. Yeo, Y. K. Ong, D. Balakrishnan, C. M. A. Limpo, A. Datta, C. Cetin, S. C. Ning, C. Wong, J. Shi, F. C. Hou, J. H. Lin, T. Minamikawa, T. Ito, H. Kamisuki, S. Pennycook, P. Matsudaira, B. Özyilmaz, *Adv. Mater.* **2024**, *36*, 2402628.

[2] a) P. Tang, W. Y. Tan, F. Z. Li, S. Xue, Y. H. Ma, P. W. Jing, Y. H. Liu, J. Zhu, X. B. Yan, *Adv. Mater.* **2023**, *35*, 2209186; b) Q. Q. Yao, P. Tang, S. Y. Xie, Y. C. Chen, Q. Y. Dou, J. Zhu, X. B. Yan, *Adv. Funct. Mater.* **2024**, *34*, 2314962; c) B. L. Sun, N. Wang, X. C. Xie, L. Zhong, L. X. He, M. L. Xiang, K. Liang, W. C. Hu, *Angew. Chem., Int. Ed.* **2024**, *63*, 202408569; d) A. M. M. Hasan, S. Bose, R. Roy, J. D. Marquez, C. Sharma, J. C. Nino, K. O. Kirlikovali, O. K. Farha, A. M. Evans, *Adv. Mater.* **2024**, *36*, 2405924.

[3] a) J. Du, Q. Han, Y. Chen, M. Peng, L. Xie, A. Chen, *Angew. Chem., Int. Ed.* **2024**, *63*, 202411066; b) J. X. Li, J. Kossmann, K. Zeng, K. Zhang, B. J. Wang, C. Weinberger, M. Antonietti, M. Odziomek, N. López-Salas, *Angew. Chem., Int. Ed.* **2023**, *135*, 202217808; c) S. J. Guan, J. X. Li, Y. Y. Wang, Y. Yang, X. Zhu, D. D. Ye, R. Chen, Q. Liao, *Adv. Mater.* **2023**, *35*, 2304465.

[4] K. S. W. Sing, D. H. Everett, R. A. W. Haul, L. Moscou, R. A. Pierotti, J. Rouquerol, T. Siemieniewska, *Pure Appl. Chem.* **1985**, *57*, 603.

[5] J. S. Huang, B. G. Sumpter, V. Meunier, *Angew. Chem., Int. Ed.* **2008**, *120*, 530.

[6] a) D. K. Singh, K. S. Krishna, S. Harish, S. Sampath, M. Eswaramoorthy, *Angew. Chem., Int. Ed.* **2016**, *55*, 2032; b) H. Jiang, J. Ma, C. Z. Li, *Adv. Mater.* **2012**, *24*, 4197.

[7] J. Chmiola, G. Yushin, Y. Gogotsi, C. Portet, P. Simon, P. L. Taberna, *Science* **2006**, *313*, 1760.

[8] a) H. R. Li, Z. T. Wu, X. C. Liu, H. T. Lu, W. C. Zhang, F. B. Li, H. Y. Yu, J. Y. Yu, B. Y. Zhang, Z. X. Xiong, Y. Tao, Q. H. Yang, *Nati. Sci. Rev.* **2024**, *11*, nwae207; b) M. R. Zhang, T. Z. Xu, D. Wang, T. Y. Yao, Z. M. Xu, Q. S. Liu, L. F. Shen, Y. Yu, *Adv. Mater.* **2023**, *35*, 2209963.

[9] J. Yin, W. L. Zhang, N. A. Alhebshi, N. Salah, H. N. Alshareef, *Small Methods* **2020**, *4*, 1900853.

[10] a) Z. J. Fan, Y. Liu, J. Yan, G. Q. Ning, Q. Wang, T. Wei, L. J. Zhi, F. Wei, *Adv. Energy Mater.* **2012**, *2*, 419; b) H. W. Liang, W. Wei, Z. S. Wu, X. L. Feng, K. Müllen, *J. Am. Chem. Soc.* **2013**, *135*, 16002.

[11] a) Y. Liu, Z. R. Wang, W. Teng, H. W. Zhu, J. X. Wang, A. A. Elzatahry, D. Al-Dahyan, W. Li, Y. H. Deng, D. Y. Zhao, *J. Mater. Chem. A* **2018**, *6*, 3162; b) J. Wei, D. D. Zhou, Z. K. Sun, Y. H. Deng, Y. Y. Xia, D. Y. Zhao, *Adv. Funct. Mater.* **2013**, *23*, 2322.

[12] a) Y. J. Li, G. L. Wang, T. Wei, Z. J. Fan, P. Yan, *Nano Energy* **2016**, *19*, 165; b) Z. Ling, Z. Y. Wang, M. D. Zhang, C. Yu, G. Wang, Y. F. Dong, S. H. Liu, Y. W. Wang, J. S. Qiu, *Adv. Funct. Mater.* **2016**, *26*, 111.

[13] a) L. Ai, W. J. Xiang, J. P. Xiao, H. M. Liu, J. K. Yu, L. L. Zhang, X. T. Wu, X. L. Qu, S. Y. Lu, *Adv. Mater.* **2024**, *36*, 2401220; b) J. Li, H. Zhou, S. Jin, B. Xu, Q. Teng, C. H. Li, J. S. Li, Q. J. Li, Z. H. Gao, C. F. Zhu, Z. F. Wang, W. Su, F. L. Yuan, *Adv. Mater.* **2024**, *36*, 2401493; c) Q. Cheng, T. Zhang, Q. Wang, X. Wu, L. Li, R. Lin, Y. Zhou, S. Qu, *Adv. Mater.* **2024**, *36*, 2408685.

[14] a) Y. M. Liu, S. Roy, S. Sarkar, J. Q. Xu, Y. F. Zhao, J. J. Zhang, *Carbon Energy* **2021**, *3*, 795; b) S. Li, L. Li, H. Y. Tu, H. Zhang, D. S. Silvester, C. E. Banks, G. Q. Zou, H. S. Hou, X. B. Ji, *Mater. Today* **2021**, *51*, 188.

[15] L. B. Tang, R. B. Ji, X. M. Li, G. X. Bai, C. P. Liu, J. H. Hao, J. Y. Lin, H. X. Jiang, K. S. Teng, Z. B. Yang, S. P. Lau, *ACS Nano* **2014**, *8*, 6312.

[16] L. Li, Y. T. Li, Y. Ye, R. T. Guo, A. N. Wang, G. Q. Zou, H. S. Hou, X. B. Ji, *ACS Nano* **2021**, *15*, 6872.

[17] a) J. S. Wei, C. Ding, P. Zhang, H. Ding, X. Q. Niu, Y. Y. Ma, C. Li, Y. G. Wang, H. M. Xiong, *Adv. Mater.* **2019**, *31*, 1806197; b) E. Raymundo-Piñero, K. Kierzek, J. Machnikowski, F. Béguin, *Carbon* **2006**, *44*, 2498; c) X. Hu, G. B. Zhong, J. W. Li, Y. J. Liu, J. Yuan, J. X. Chen, H. B. Zhan, Z. H. Wen, *Energy Environ. Sci.* **2020**, *13*, 2431.

[18] a) G. L. Zhang, T. T. Guan, J. L. Qiao, J. L. Wang, K. X. Li, *Energy Storage Mater.* **2020**, *26*, 119; b) T. X. Shang, Y. Xu, P. Li, J. W. Han, Z. T. Wu, Y. Tao, Q. H. Yang, *Nano Energy* **2020**, *70*, 104531.

[19] Y. Zheng, W. Zhang, X. B. Zhu, F. X. Liu, C. M. Yang, W. T. Zheng, *J. Am. Chem. Soc.* **2024**, *146*, 20291.

[20] J. N. Xu, J. Y. Tang, Y. Shi, J. J. Xie, F. Lei, L. C. Fan, L. Zhang, *Appl. Surf. Sci.* **2024**, *670*, 160551.

[21] X. Y. Li, C. C. Cai, L. Zhou, L. Q. Mai, H. J. Fan, *Adv. Mater.* **2024**, *36*, 2404393.

[22] L. N. Han, X. Wei, Q. C. Zhu, S. M. Xu, K. X. Wang, J. S. Chen, *J. Mater. Chem. A* **2016**, *4*, 16698.

[23] D. H. Tang, T. Wang, W. T. Zhang, Z. Zhao, L. Zhang, Z. A. Qiao, *Angew. Chem., Int. Ed.* **2022**, *61*, 202203967.

[24] P. Han, M. S. Cheng, D. H. Luo, W. Cui, H. C. Liu, J. G. Du, M. L. Wang, Y. P. Zhao, L. Chen, C. Z. Zhu, J. Xu, *Energy Storage Mater.* **2020**, *24*, 486.

[25] a) J. Huang, C. Liu, Y. Z. Jin, J. C. Chen, *Chem. Eng. J.* **2023**, *461*, 141930; b) N. F. Yu, H. Chen, J. B. Kuang, K. L. Bao, W. Yan, J. L. Ye, Z. T. Yang, Q. H. Huang, Y. P. Wu, S. G. Sun, *Nano Res.* **2022**, *15*, 7209.

[26] a) R. Zhang, X. X. Jing, Y. T. Chu, L. Wang, W. J. Kang, D. H. Wei, H. B. Li, S. L. Xiong, *J. Mater. Chem. A* **2018**, *6*, 17730; b) Y. C. Liu, M. J. Shi, M. N. Han, J. Yang, J. H. Yu, M. Narayanasamy, K. Dai, S. Angaiah, C. Yan, *Chem. Eng. J.* **2020**, *387*, 124104.

[27] J. Li, Z. H. Xia, X. W. Wang, C. Feng, Q. C. Zhang, X. A. Chen, Y. Yang, S. Wang, H. L. Jin, *Adv. Mater.* **2024**, *36*, 2310422.

[28] a) Z. Y. Song, D. Z. Zhu, L. C. Li, T. Chen, H. Duan, Z. W. Wang, Y. K. Lv, W. Xiong, M. X. Liu, L. H. Gan, *J. Mater. Chem. A.* **2019**, *7*, 1177; b) S. Ghosh, S. Barg, S. M. Jeong, K. Ostrikov, *Adv. Energy Mater.* **2020**, *10*, 2001239.

[29] H. Chen, T. Liu, J. R. Mau, W. J. Zhang, Z. J. Jiang, J. Liu, J. L. Huang, M. L. Liu, *Nano Energy* **2019**, *63*, 103836.

[30] a) C. F. Ding, T. Y. Liu, X. D. Yan, L. B. Huang, S. O. Ryu, J. L. Lan, Y. H. Yu, W. H. Zhong, X. P. Yang, *Nano-Micro Lett.* **2020**, *12*, 63; b) A. Gopalakrishnan, S. Badhulika, *J. Power Sources* **2020**, *480*, 228830.

[31] B. W. Chen, W. Z. Wu, C. Y. Li, Y. F. Wang, Y. Zhang, L. J. Fu, Y. S. Zhu, L. X. Zhang, Y. P. Wu, *Sci. Rep.* **2019**, *9*, 5431.

[32] H. Z. Sun, M. J. Xiao, F. L. Zhu, *J. Electroanal. Chem.* **2023**, *932*, 117254.

[33] Q. Xiong, B. Liu, Y. Liu, P. Wang, H. Cheng, H. Li, Z. Lu, M. Yang, *Nano Res.* **2022**, *15*, 7759.

[34] Z. Shang, X. Y. An, H. Zhang, M. X. Shen, F. Baker, Y. X. Liu, L. Q. Liu, J. Yang, H. B. Cao, Q. L. Xu, H. B. Liu, Y. H. Ni, *Carbon* **2020**, *161*, 62.

© 2024 Wiley-VCH GmbH

16163028, 2025, 16, Downloaded from https://advanced.onlinelibrary.wiley.com/doi/10.1002/adfm.202419219 by Fudan University, Wiley Online Library on [23/04/2025]. See the Terms and Conditions (https://onlinelibrary.wiley.com/terms-and-conditions) on Wiley Online Library for rules of use; OA articles are governed by the applicable Creative Commons License